Microwave Vortex Beam Lasing via Photonic Time Crystals

Lei Huang,[1,*] Weixuan Zhang,[1,*,†] Deyuan Zou,[1] Jiacheng Bao,[2] Fengxiao Di,[1] Haoyu Qin,[1] Long Qian,[1] Houjun Sun,[2,‡] and Xiangdong Zhang[1,§]

[1]*Key Laboratory of Advanced Optoelectronic Quantum Architecture and Measurements of Ministry of Education, Beijing Key Laboratory of Nanophotonics and Ultrafine Optoelectronic Systems, School of Physics, Beijing Institute of Technology, 100081 Beijing, China*

[2]*Beijing Key Laboratory of Millimeter Wave and Terahertz Techniques, School of Information and Electronics, Beijing Institute of Technology, Beijing 100081, China*

(Received 14 January 2026; revised 20 March 2026; accepted 27 May 2026; published 7 July 2026)

Microwave lasing carrying orbital angular momentum (OAM) holds significant potential for advanced applications in fields such as high-capacity communications, precision sensing, and radar imaging. However, conventional approaches to masers fail to produce emission with embedded OAM. The recent emergence of photonic time crystals (PTCs)—artificially structured media with periodically varying electromagnetic properties in time—offers a paradigm shift toward resonance-free lasing without the need for gain media. Yet, pioneering PTC designs have been based on three-dimensional bulk structures, which lack a surface-emitting configuration, and do not possess the capability to modulate OAM, thus hindering the realization of surface-emitted PTC masing that carries OAM. Here, we report the first experimental demonstration of surface-emitted microwave vortex beam lasing using ring-shaped PTCs, without the need for either a gain medium or a high-Q cavity. By developing a multiplier-driven time-varying metamaterial that achieves over 100% equivalent permittivity modulation depth, we establish momentum band gaps (k gaps) with sufficient bandwidth to overcome intrinsic losses and enable self-sustained coherent microwave amplification. Furthermore, space-time modulation induces nonreciprocity between clockwise and counterclockwise *k-gap* modes within the circularly symmetric PTC structure, facilitating the selective generation of microwave lasing carrying OAM, a functionality that is not readily accessible in conventional maser architectures. Our Letter bridges PTC physics with coherent OAM-carrying microwave emission, establishing a transformative platform for next-generation wireless communications, advanced sensing systems, and OAM-based technologies.

DOI: 10.1103/6gn2-2v9b

Time-varying media have emerged as a transformative paradigm across wave physics [1–8]. Unlike static systems, dynamically modulated materials exhibit extraordinary phenomena and enable functionalities that are fundamentally unattainable in conventional platforms. Photonic time crystals (PTCs) [9–15], characterized by periodic temporal modulation of electromagnetic parameters, have garnered significant interest. Their unique interplay of temporal reflections and refractions generates momentum band gaps (k gaps), enabling exotic phenomena like momentum-selective dynamical gain [15], topological phase transitions in k gaps [16–18], and others [19–31]. Critically, PTCs theoretically support nonresonant and gain medium-free lasing via amplification [15], a revolutionary departure from high-Q cavity-dependent lasers that could transcend traditional gain-medium limitations. However, translating this principle into practice faces challenges, particularly at optical frequencies, where prohibitive modulation speeds and amplitudes are required.

Meanwhile, masers [32], the microwave precursors to lasers [33–36], persist in specialized applications such as deep-space communications and quantum technologies. Their broader impact remains constrained by inherent limitations: conventional designs rely on high-Q cavities and restrictive gain media, leading to narrow frequency tunability and suboptimal energy efficiency. Operational requirements for low temperatures, high-vacuum environments, and intense magnetic fields [37–43] further hinder practical deployment. Moreover, traditional masing schemes have been confined to unstructured fields, lacking functionalities for generating microwave lasing carrying orbital angular momentum (OAM). This raises a pivotal question: can PTC physics bypass these constraints to enable surface-emitted microwave radiation with a structured OAM wavefront? In fact, realizing this PTC-driven microwave lasing also faces great difficulties. A pioneering work revealed

[*]These authors contributed equally to this work.
[†]Contact author: zhangwx@bit.edu.cn
[‡]Contact author: sunhoujun@bit.edu.cn
[§]Contact author: zhangxd@bit.edu.cn

non-Hermitian band structures of photonic Floquet media using varactor diodes inside a closed metallic waveguide [28], where noise-initiated microwave oscillations originating from k-gaps have been observed. Based on a similar design, the spontaneous-emission analogs and a lasing transition have also been achieved in PTCs [31]. However, the closed structure of PTC inherently prevents out-of-plane emission with structured wavefront. In addition, an open-structure PTC has demonstrated microwave far-field amplification [30]. Nevertheless, owing to the limited modulation strength achievable with varactor diodes, achieving robust k-gap-driven lasing accompanied by a controllable structured wave front remains challenging. These considerations motivate the following question: can one design an open PTC platform that exploits k-gap amplification to realize surface-emitted microwave lasing carrying OAM?

In this Letter, we demonstrate surface-emitted microwave vortex-beam lasing enabled by a PTC platform in an open configuration. We develop a multiplier-driven time-varying capacitance architecture that delivers 100% equivalent permittivity modulation depth, activating robust momentum-gap amplification. Full-wave simulations and experiments demonstrate threshold-governed maserlike emission from PTCs in both near- and far-field regions. Notably, space-time modulation induces symmetry breaking that generates vortex-beam masing carrying OAM. Our Letter establishes a unified framework integrating PTC physics with maser engineering, creating a new paradigm for various microwave applications.

Theory of surface-emitted microwave lasing with OAM via spatiotemporal PTCs—Pioneering works on PTC lasing were limited to bulk structures without angular modulation [15], hindering the surface emission and OAM generation. Here, we design a ring-shaped PTC confined in a two-dimensional surface to overcome these limitations. Figure 1(a) illustrates the conceptual design, where a ring-shaped (radius R) spatiotemporally modulated surface capacitance enables surface-emitting microwave lasing with OAM. The surface capacitance $C(\phi,t) = C_0[1+\delta\cos(q\phi-\Omega t)]$ (the bottom chart) exhibits the rotational space-time symmetry $C(\phi,t) = C[\phi+\theta, t+(q\theta/\Omega)]$, where $[\theta,(q\theta/\Omega)]$ is the space-time rotational vector, $\phi\in[0,2\pi)$ is the angular coordinate, Ω is the modulation frequency and integer q governs the angular periodicity. We can expand $C(\phi,t)$ as $C(\phi,t) = \sum_m c_m e^{im(q\phi-\Omega t)}$ ($m\in Z$). We assume that transverse electric waves propagate along the ϕ direction. Thus, electric field (E_ρ) is radially polarized, and magnetic field comprises azimuthal (H_ϕ) and vertical (H_z) components. Based on the Floquet-Bloch theory, the eigenwaves take the form as

$$\begin{cases} E_\rho = \sum_n E_{\rho,n} e^{-\gamma_n z} e^{i[(p+nq)\phi-(\omega+n\Omega)t]}, \\ H_\phi = \sum_n H_{\phi,n} e^{-\gamma_n z} e^{i[(p+nq)\phi-(\omega+n\Omega)t]}, \\ H_z = \sum_n H_{z,n} e^{-\gamma_n z} e^{i[(p+nq)\phi-(\omega+n\Omega)t]}, \end{cases} \quad (1)$$

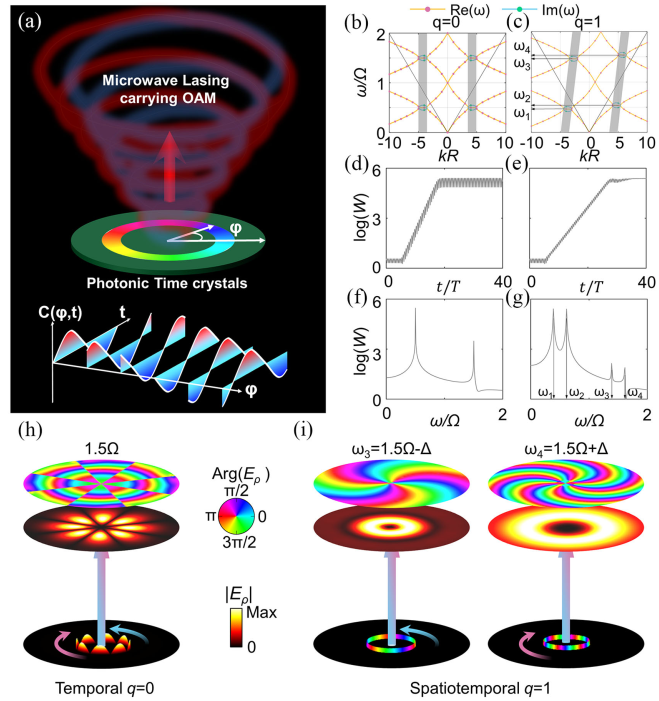

FIG. 1. Theory of surface-emitted OAM lasing via spatiotemporal PTCs. (a) Schematic of the ring-shaped PTC with modulated surface capacitance $C(\phi,t)$. (b),(c) Eigenenergy spectra for temporal ($q=0$) and spatiotemporal ($q=1$) modulations. Dots: discrete eigenmodes; yellow curves: infinite PTC band dispersion. (d)–(g) Time-domain evolution (d), (e) and Fourier spectra (f), (g) of near-field responses under $q=0$ and $q=1$, showing saturation and spectral splitting. (h),(i) Far-field amplitude and phase distributions at dominant frequencies, indicating zero OAM for $q=0$ and helical phases for $q=1$. Parameters: $R=0.4$ m, $\Omega/2\pi = 634$ MHz, $C_0 = 2$ pF, $\delta = 0.1$.

where γ_n represents the radiation rate of eigenwaves toward background. p is related to wave vector k by $p = kR$. ω defines the eigenfrequency. Substituting Eq. (1) into a free-space Maxwell's equation and surface-capacitance boundary condition, we can solve the eigenspectra of the ring-shaped PTC (see details in S1 of Supplemental Material [44]). Figures 1(b) and 1(c) present calculated eigenspectra for temporal ($q=0$) and spatiotemporal ($q=1$) modulations. Other parameters are applied in the figure caption. We find that ring-shaped PTCs possess equally spaced eigenmodes due to angular periodicity, where the system with a larger circumference possesses more discrete eigenmodes. It is shown that both temporal and spatiotemporal modulations can introduce k) gaps (shaded areas), which sustain gain modes enabling coherent amplification. For comparison, we also plot band dispersions of a spatial infinite PTC characterized by $C(x,t) = C_0[1+\delta\cos(Kx-\Omega t)]$ with $K = q/R$, as shown by solid lines. It is seen that discrete eigenmodes of ring-shaped PTCs are embedded within the band dispersion of infinite PTCs. In addition, it is worth noting that, under temporal modulation, the system preserves continuous rotational symmetry, resulting in identical dispersion bands for clockwise (CW) and counterclockwise (CCW) propagating eigen-waves. In contrast, spatiotemporal modulation breaks the reciprocity, yielding asymmetric dispersion curves for opposite wavevectors. This asymmetry confirms the nonreciprocal nature of space-time modulated systems, where CW and CCW k-gap eigenmodes exhibit distinct frequencies ($\omega_1 \neq \omega_2$ and $\omega_3 \neq \omega_4$).

To further illustrate PTC-enabled microwave lasing, Figs. 1(d) and 1(g) depict the wave evolution and Fourier spectrum of a near-field point under temporal and spatiotemporal modulations. The detailed simulation method can be found in S2 of [44]. For temporal modulation, the initial exponential growth of electric field appears and saturates into a steady state. The Fourier spectrum reveals eigenmodes at odd multiples of 0.5 Ω, being aligned with eigenenergies. Under spatiotemporal modulation, the field similarly exhibits exponential growth followed by saturation. While the Fourier spectrum splits into nondegenerate peaks ($0.5\ n\Omega \pm \Delta$, n is odd number) in each Floquet sector, corresponding to CW and CCW k-gap eigenmodes. This is consistent with the asymmetric band structure with respect to the k vector in Fig. 1(c). Then, we investigate far-field radiation of surface-emitted masing fields in both temporal and spatiotemporal PTCs. Far-field radiation is calculated using angular spectrum theory (see S3 of Supplemental Material [44] for details). Figure 1(h) depicts the near-field distribution (lower panel), and the far-field phase and amplitude distributions (upper panels) of E_ρ at 1.5 Ω under temporal modulation. The near field exhibits a standing-wave pattern due to the simultaneous excitation of degenerate CW and CCW modes. As this pair of degenerate modes generate OAM beams with opposite topological charges, the total far-field radiation carries zero OAM. In contrast, spatiotemporal modulation breaks reciprocity of CW and CCW modes. Two charts in Fig. 1(i) present near- and far-field distributions for the spatiotemporal case at $1.5\ \Omega - \Delta$ and $1.5\ \Omega + \Delta$. It is shown that far-field phase profiles display spiral structures with 6 and −3 topological charges related to CW and CCW modes at $1.5\ \Omega + \Delta$ and $1.5\ \Omega - \Delta$, confirming the generation of coherent microwave emission with OAMs. In S4 of [44], we further explore the impact of circumference on the divergence angle of microwave lasing, demonstrating size-enhanced directivity. It is crucial to emphasize that, in contrast to conventional approaches relying on high-Q whispering-gallery-mode resonances to achieve lasing through strong light-gain medium interactions [56], our system eliminates the need for cavity and gain medium. Instead, the self-sustained amplification arises from k-gap modes and the ring-shape surface geometry is used to enable the vertical emission with OAMs.

Implementation of surface-emitted microwave lasing with OAM by spatiotemporal metamaterials—To experimentally realize surface-emitted microwave lasing with

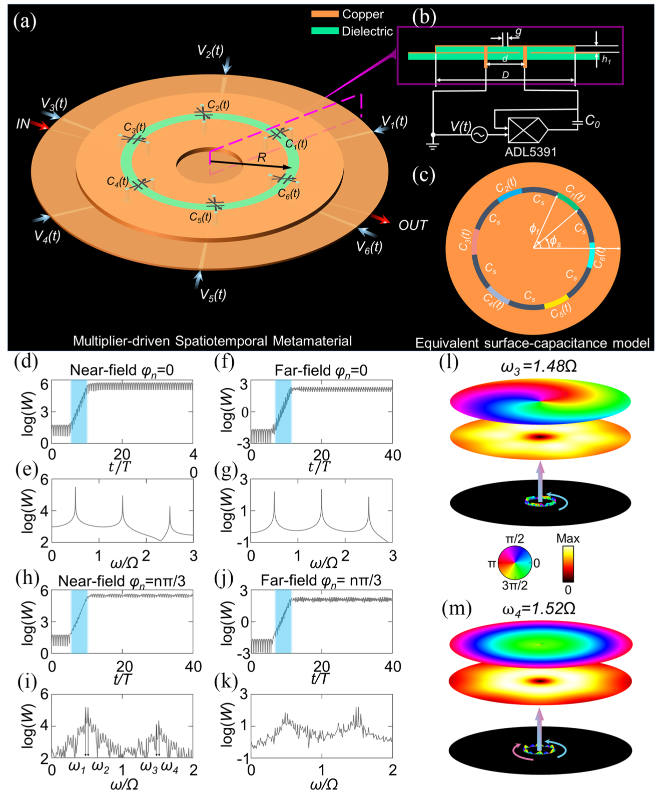

FIG. 2. Multiplier-driven spatiotemporal metamaterial and OAM lasing. (a) Top-view schematic of the ring-shaped waveguide with six time-varying capacitance units. (b) Cross section with substrate and control circuit (inset: multiplier and fixed capacitor). (c) Discretized surface-capacitance model. (d),(e) Near-field intensity evolution and spectrum under temporal modulation ($\varphi_n = 0$). (f),(g) Far-field counterparts. (h),(i) Near-field and (j),(k) far-field results under spatiotemporal modulation ($\varphi_n = n\pi/3$), showing spectral splitting. (l),(m) Far-field phase profiles at split frequencies, confirming OAM states (phase scale: 0–2π). Simulation: $\omega/2\pi = 304$ MHz, $\Omega/2\pi = 608$ MHz, $R = 0.1$ m.

OAMs, we design multiplier-driven time-varying metamaterial to emulate the spatiotemporal surface-capacitance model. Our method can overcome intrinsic limitations using varactor diodes (see S5 of Supplemental Material [44]). As depicted in Fig. 2(a), a ring-shaped gap (with radius R and width g) is etched into the top metal plane (orange) to form a planar waveguide, which is coupled with a few multiplier-driven time-varying capacitors. Figure 2(b) shows the cross-section structure. In the multiplier-driven time-varying capacitor, the microwave multiplier receives an external modulation signal $V_n(t)$ ($n = [1, 6]$) at one input port and the other couples to the planar waveguide. The output port of multiplier connects in series with a fixed capacitor C_0 and feeds back to the planar waveguide. Leveraging the multiplier function, we achieve an effective time-varying capacitance $C = C_0[1 - V(t)]$ (see details in S6 of [44]). Our multiplier-driven approach offers three key advantages: 100% modulation depth (enabling larger

k gaps), linear modulation under large voltages, and the isolation between modulation and propagation signals. Unlike the idealized surface-capacitance model, the ring-shaped planar waveguide exhibits significant frequency dispersion, which constrains the operational bandwidth of PTCs. Therefore, we must design PTCs to ensure that the fundamental k-gap eigenmode at 0.5 Ω resides within the band- pass region. Our multiplier-driven metamaterial can generate a sufficiently large k gap, leading to coherent microwave amplification.

To implement spatiotemporal PTCs, we integrate six multiplier-driven capacitance modules around ring-shaped planar waveguide, being equivalent to the discretized surface-capacitance model in Fig. 2(c). Each colored segment with $\phi \in [\phi_s + n\pi/3, \phi_f + n\pi/3]$ $(n \in [1, 6])$ corresponds to a uniform time-varying capacitive region associated with a multiplier module. Different colors represent $C_n(t) = C_p + C_{\mathrm{mod}} \sin(2\omega t + \varphi_n)$ with distinct phases φ_n, which is designed to match $q\phi$ of the continuous spatiotemporal modulation. Between each pair of time-varying capacitor modules, the surface capacitance C_s is applied, representing the inherent capacitance of planar waveguide segments connecting modulated modules. We can determine effective values of C_p, C_{mod}, C_s, ϕ_s, and ϕ_f for time-varying and static effective capacitances from simulations (see S7 of Supplemental Material [44]). These values are then used to define the discretized spatiotemporal surface capacitance model for full-wave simulations. The simulated wave evolutions and frequency spectra under temporal modulation ($\varphi_n = 0$) at near- and far-field points are shown in Figs. 2(d)–2(g). Other parameters are presented in the figure caption. It is shown that both near- and far-field waves exhibit exponential growth, saturating to steady states due to the multiplier output limit. Spectral peaks appear at ω, 3ω, 5ω, which match to k-gap eigenfrequencies in the continuous counterpart. Notably, while the ideal surface-capacitance model [Fig. 1(a)] places the 3ω-component eigenmode below the light line, the discretized capacitance distribution transforms the continuously rotational symmetry to discrete rotational symmetry, which can couple the 3ω-mode's wave vector above the light line [57], as evident by the larger far-field radiation intensity (see S8 of [44] for details).

Finally, we investigate the masing behavior in spatiotemporal PTC metamaterials by configuring the modulation phase as $\varphi_n = n\pi/3$ $(n \in [1, 6])$. The calculated near-field [Fig. 2(h)] and far-field [Fig. 2(j)] evolutions again show exponential growths followed by saturation. The corresponding frequency spectra in Figs. 2(i) and 2(k) reveal the spectral splitting in each Floquet sector. The oscillation feature of frequency spectra originates from discretized spatiotemporal modulation. This splitting behavior is consistent with the prediction of the continuous surface-capacitance model [Fig. 1(g)]. It is important to emphasize a key distinction from the continuous case: in the continuous limit, CW and CCW k-gap modes are fully decoupled. However, the spatial discretization in the practical design introduces the coupling between these two eigenmodes. Consequently, two split components no longer correspond purely to CW and CCW eigenmodes, but rather represent superposition of both. The coupling coefficients governing this superposition depend on the density of time-varying capacitor modules, the circumference and impedance of ring-shaped PTC (see S9 of Supplemental Material [44]). To further characterize OAM properties of two split eigenmodes in spatiotemporal PTCs, we compute far-field radiation patterns at $\omega_1 = 1.48$ Ω and $\omega_2 = 1.52$ Ω, as shown in Figs. 2(l) and 2(m). Because of the strong near-field coupling between CW and CCW eigenmodes at $\omega_2 = 1.52$ Ω, the nonchiral wave profile appears, preventing its OAM properties in the far field. In contrast, the CCW-dominated near-field profile still exists at $\omega_1 = 1.48$ Ω, resulting in a helical phase with topological charge being -1 in the far-field region. It is worth noting that by suitably engineering the structural parameters, we can make two split eigenmodes become dominated either by the CW or CCW mode (see S9 of Supplemental Material [44]). Furthermore, as the number of discrete modulation units increases, the lasing related parameters progressively converge toward constant values, corresponding to the limit of continuous modulation (see S10 of [44]).

Experimental observation of surface-emitted microwave lasing carrying OAM—Building on the theoretical framework, we fabricate designed spatiotemporal metamaterials with $R = 0.1$ m, $g = 1$ mm and six multiplier-driven capacitance modules, as shown in Figs. 3(a) and 3(b) for front and back views. The enlarged inset details a time-varying capacitance module (see S11 of Supplemental Material [44] for fabrication details). At first, we apply the homogenous modulation signal, $(t) = V_{\mathrm{mod}} \sin(2\omega t)$ with $\omega/2\pi = 208$ MHz and $V_{\mathrm{mod}} = 0.45$ V, to all modulation ports (blue arrows) to observe temporal PTC-enabled coherent microwave emission. We measure the wave evolution at the output port (the red arrow) and plot the corresponding frequency spectrum in Fig. 3(c). It is shown that the frequency spectrum exhibits dominant peaks at ω, 3ω, and 5ω, confirming that k-gap modes govern the evolution in temporal PTC. Furthermore, we measure the frequency spectrum at a far-field point located at $z = 1$ m from the PTC structure, as shown in Fig. 3(d). The ω mode remains dominant in the far-field radiation, being different from the 3ω-mode dominated far-field emission shown in Fig. 2(g). This is attributed to the breaking of C_6 symmetry in the fabricated sample (see S12 of Supplemental Material [44] for details).

To further investigate the threshold behavior of microwave lasing in PTCs, we characterize the steady-state intensities versus the modulation voltage for both near- [Fig. 3(e)] and far-field [$z = 1$ m, Fig. 3(f)] regions. When $V_{\mathrm{mod}} < 0.37$ V, both intensities remain below the detection

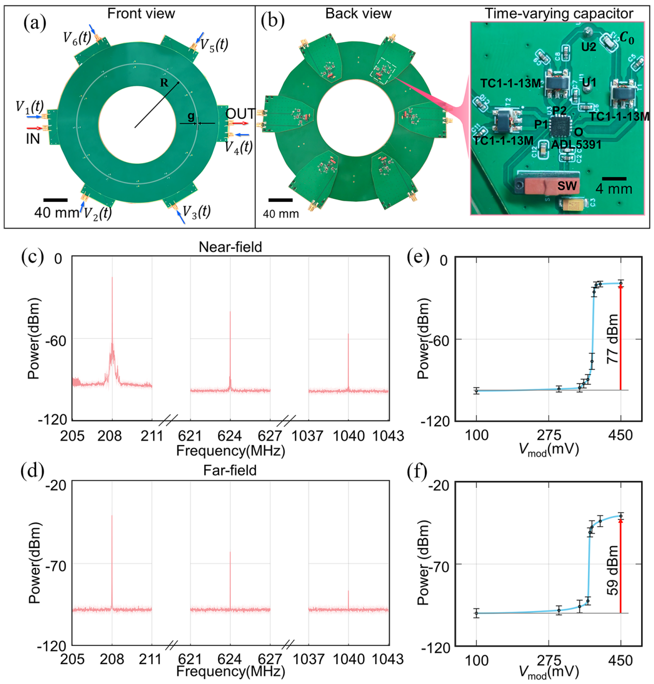

FIG. 3. Experimental temporal PTC lasing. (a),(b) Fabricated metamaterial front and back views, with ring waveguide ($R = 0.1$ m, $g = 1$ mm) and six multiplier-driven modules. Inset: single module schematic. (c) Near-field spectrum showing peaks at ω, 3ω, 5ω ($\omega/2\pi = 208$ MHz). (d) Far-field spectrum at 1 m distance. (e),(f) Threshold behavior of near-field (e) and far-field (f) intensities versus V_{mod}, with threshold at 0.37 V.

limit. This indicates a loss-dominant regime after removing the excitation signal, where the k gap is insufficient to overcome absorption and radiation losses. For $V_{\mathrm{mod}} > 0.37$ V, both near- and far-field intensities surge to saturation levels, demonstrating the self-sustained microwave lasing in PTCs. Our experimental results establish that the multiplier-driven time-varying metamaterial achieves sufficient modulation to open large k gaps to overcome intrinsic losses, enabling the self-sustained coherent microwave amplification. The corresponding phase noise has been characterized and shows the relatively stable spectral performance (see S13 of [44]).

Lastly, we implement the spatiotemporal PTCs by configuring the phases of six modulation signals as $\varphi_n = n\pi/3$ ($n \in [1, 6]$). Figures 4(a) and 4(b) display measured frequency spectra at near- and far-field locations with $V_{\mathrm{mod}} = 0.5$ V. It is found that two frequency spectra exhibit significant frequency splitting. This phenomenon aligns with the full-wave simulation of the discretized surface-capacitance model. Moreover, the frequency components in the low-transmission region are accompanied by strong propagation loss and are buried in the background noise, rendering the oscillatory feature in Fig. 2(i) unobservable in experimental measurements. Figures 4(c) and 4(d) present the steady-state intensities at near- and far-field points versus V_{mod} . We find that, below the masing

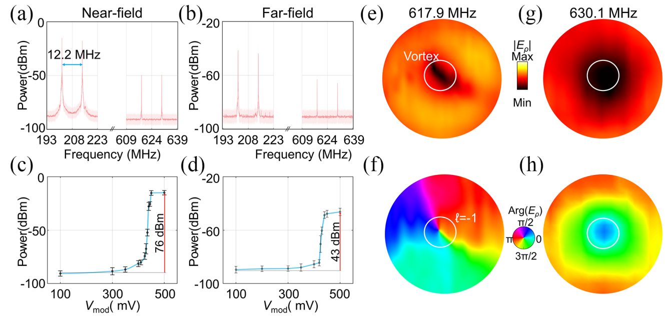

FIG. 4. Experimental spatiotemporal PTC lasing with OAM. (a) Near-field spectrum showing frequency splitting ($f_1 = 201.9$, $f_2 = 214.1$, $\Delta f = 12.2$ MHz under $\varphi_n = n\pi/3$ ($n \in [1, 6]$). (b) Far-field spectrum confirms splitting. (c) Measured max power versus V_{mod}, showing threshold at 0.44 V. (d) Near and far-field intensities versus V_{mod}, indicating threshold-triggered amplification. (e),(f) Far-field intensity and phase at 617.9 MHz, showing spiral phase with topological charge -1. (g),(h) Corresponding distributions at 630.1 MHz, without helical phase.

threshold, field intensities remain minimal below the detection limit. While, when V_{mod} exceeds the threshold of 0.44 V, the steady-state intensities exhibit steplike jumps.

Then, we measure far-field intensity and phase distributions of the E_ρ component, as shown in Figs. 4(e) and 4(f) for 617.9 MHz and Figs. 4(g) and 4(h) for 630.1 MHz. Consistent with theoretical predictions, the mode coupling between CW and CCW components occurs, resulting in a hybridization between CW and CCW modes at two spectral peaks. At 617.9 MHz, the coupling is relatively weak, which allows the dominant features of the CW mode to remain preserved: a toroidal intensity null at the beam center and a spiral phase distribution. Such beam exhibits a purity of 77.29% of OAMs with -1 topological charge, which is comparable to that with other OAM generation methods (see S14 of Supplemental Material [44]). At 630.1 MHz, the strong CW-CCW coupling suppresses the spiral phase distribution. These results agree with simulations in Figs. 2(l) and 2(m). It is noted that the purity of the generated OAM beam is mainly limited by the discretization of the modulation profile, phase and amplitude errors among units, and variations between electronic modules, which introduce mode mixing. Further improvements in modulation unit number, phase synchronization, and module uniformity could enhance the OAM purity in PTC masing.

We quantify the contributions of ohmic, radiation, and multiplier losses in our system to determine the resulting radiative energy conversion efficiency (see S15 of [44] for details). This efficiency is significantly higher than that of conventional and OAM masers, primarily because the present PTC platform avoids the inefficient population-inversion processes and associated dissipation typical of conventional gain media-based systems.

Conclusion—In conclusion, we have realized the first surface-emitted microwave lasing with OAMs through spatiotemporal PTCs. We extend PTC-lasing model from the bulk-temporal modulation to surface-spatiotemporal modulation, enabling out-of-plane PTC masing with OAMs. In experiments, we propose a multiplier-based time-varying capacitor, achieving nearly an order of magnitude enhancement in modulation strength compared to existing approaches. The generated k gap can overcome both transmission and out-of-plane radiation losses, enabling surface-emitted OAM masing. We note that PTC masing can generate high-frequency emission using a low-frequency driving signal. This mechanism is more efficient than traditional approaches relying on material nonlinearities [58]. While demonstrated in the GHz range with low-order OAM modes, the proposed scheme is expected to extended to higher frequencies and higher-order OAM modes by employing higher-frequency modulation components, increasing the number of spatiotemporal modulation units, and reducing system losses. In addition, unlike conventional and OAM masers (see S16 of Supplemental Material [44]), our platform encodes topological information directly into masing fields, while exhibiting higher energy efficiency, comparable mode purity, and enhanced tunability in both frequency and OAM order, thereby establishing a new framework for integrating PTCs with microwave communication and engineering.

Acknowledgments—This work is supported by the National Key R&D Program of China under Grant No. 2022YFA1404900, National Natural Science Foundation of China No. 12422411, and Beijing Natural Science Foundation No. 1242027.

Data availability—There are no publicly available research data or software supporting this manuscript. Requests for further information or data should be sent to the authors.

[1] J. Zhang *et al.*, Observation of a discrete time crystal, Nature (London) **543**, 217 (2017).
[2] E. Galiffi *et al.*, Photonics of time-varying media, Adv. Photonics **4**, 014002 (2022).
[3] N. Engheta, Four-dimensional optics using time-varying metamaterials, Science **379**, 1190 (2023).
[4] M. S. Rudner and N. H. Lindner, Band structure engineering and nonequilibrium dynamics in Floquet topological insulators, Nat. Rev. Phys. **2**, 229 (2020).
[5] S. Yin, E. Galiffi, and A. Alù, Floquet metamaterials, eLight **2**, 8 (2022).
[6] L. Yuan, Q. Lin, M. Xiao, and S. Fan, Synthetic dimension in photonics, Optica **5**, 1396 (2018).
[7] Y. Wang, B. Yousefzadeh, H. Chen, H. Nassar, G. Huang, and C. Daraio, Observation of nonreciprocal wave propagation in a dynamic phononic lattice, Phys. Rev. Lett. **121**, 194301 (2018).
[8] J. Li *et al.*, Reciprocity of thermal diffusion in time-modulated systems, Nat. Commun. **13**, 167 (2022).
[9] D. Holberg and K. Kunz, Parametric properties of fields in a slab of time-varying permittivity, IEEE Trans. Antennas Propag. **14**, 183 (1966).
[10] F. Biancalana, A. Amann, A. V. Uskov, and E. P. O'Reilly, Dynamics of light propagation in spatiotemporal dielectric structures, Phys. Rev. E **75**, 046607 (2007).
[11] J. R. Zurita-Sánchez, P. Halevi, and J. C. Cervantes-Gonzalez, Reflection and transmission of a wave incident on a slab with a time-periodic dielectric function $\epsilon(t)$, Phys. Rev. A **79**, 053821 (2009).
[12] J. R. Reyes-Ayona and P. Halevi, Observation of genuine wave vector (k or β) gap in a dynamic transmission line and temporal photonic crystals, Appl. Phys. Lett. **107**, 074101 (2015).
[13] A. M. Shaltout, J. Fang, A. V. Kildishev, and V. M. Shalaev, Photonic time-crystals and momentum band-gaps, in Conference on Lasers and Electro-Optics, OSA Technical Digest (online) (Optica Publishing Group, 2016), paper FM1D.4.
[14] M. M. Asgari, P. Garg, X. Wang, M. S. Mirmoosa, C. Rockstuhl, and V. Asadchy, Theory and applications of photonic time crystals: A tutorial, Adv. Opt. Photonics **16**, 958 (2024).
[15] M. Lyubarov, Y. Lumer, A. Dikopoltsev, E. Lustig, Y. Sharabi, and M. Segev, Amplified emission and lasing in photonic time crystals, Science **377**, 425 (2022).
[16] E. Lustig, Y. Sharabi, and M. Segev, Topological aspects of photonic time crystals, Optica **5**, 1390 (2018).
[17] Y. Ren *et al.*, Observation of momentum-gap topology of light at temporal interfaces in a time-synthetic lattice, Nat. Commun. **16**, 707 (2025).
[18] J. Feis, S. Weidemann, T. Sheppard, H. M. Price, and A. Szameit, Space-time-topological events in photonic quantum walks, Nat. Photonics **19**, 518 (2025).
[19] Dikopoltsev, Y. Sharabi, M. Lyubarov, Y. Lumer, S. Tsesses, E. Lustig, I. Kaminer, and M. Segev, Light emission by free electrons in photonic time-crystals, Proc. Natl. Acad. Sci. U.S.A. **119**, e2119705119 (2022).
[20] H. Li, S. Yin, H. He, J. Xu, A. Alù, and B. Shapiro, Stationary charge radiation in anisotropic photonic time crystals, Phys. Rev. Lett. **130**, 093803 (2023).
[21] Y. Pan, M. I. Cohen, and M. Segev, Superluminal k-gap solitons in nonlinear photonic time crystals, Phys. Rev. Lett. **130**, 233801 (2023).
[22] X. Wang, P. Garg, M. S. Mirmoosa, A. G. Lamprianidis, C. Rockstuhl, and V. S. Asadchy, Expanding momentum bandgaps in photonic time crystals through resonances, Nat. Photonics **19**, 149 (2025).
[23] Y. Sharabi, E. Lustig, and M. Segev, Disordered photonic time crystals, Phys. Rev. Lett. **126**, 163902 (2021).
[24] Y. Sharabi, A. Dikopoltsev, E. Lustig, Y. Lumer, and M. Segev, Spatiotemporal photonic crystals, Optica **9**, 585 (2022).
[25] R. Yousefjani, K. Sacha, and A. Bayat, Discrete time crystal phase as a resource for quantum-enhanced sensing, Phys. Rev. B **111**, 125159 (2025).

[26] P. A. Huidobro, E. Galiffi, S. Guenneau, R. V. Craster, and J. B. Pendry, Fresnel drag in space–time-modulated metamaterials, Proc. Natl. Acad. Sci. U.S.A. **116**, 24943 (2019).

[27] E. Galiffi, P. A. Huidobro, and J. B. Pendry, Broadband nonreciprocal amplification in luminal metamaterials, Phys. Rev. Lett. **123**, 206101 (2019).

[28] J. Park, H. Cho, S. Lee, K. Lee, K. Lee, H. C. Park, J.-W. Ryu, N. Park, S. Jeon, and B. Min, Revealing non-Hermitian band structure of photonic floquet media, Sci. Adv. **8**, eabo6220 (2022).

[29] X. Ye, Y. G. Wang, J. F. Yao, Y. Wang, C. X. Yuan, and Z. X. Zhou, Realization of spatiotemporal photonic crystals based on active metasurface, Laser Photonics Rev. **19**, 2401345 (2025).

[30] X. Wang, M. S. Mirmoosa, V. S. Asadchy, C. Rockstuhl, S. Fan, and S. A. Tretyakov, Metasurface-based realization of photonic time crystals, Sci. Adv. **9**, eadg7541 (2023).

[31] K. Lee, M. Kyung, Y. Kim, J. Park, H. Lee, J. Choi, C. T. Chan, J. Shin, K. W. Kim, and B. Min, Analogs of spontaneous emission and lasing in photonic time crystals, Phys. Rev. Lett. **136**, 093802 (2026).

[32] J. P. Gordon, H. J. Zeiger, and C. H. Townes, Molecular microwave oscillator and new hyperfine structure in the microwave spectrum of NH_3, Phys. Rev. **95**, 282 (1954).

[33] T. H. Maiman, Stimulated optical radiation in ruby, Nature (London) **187**, 493 (1960).

[34] H. G. Heard, Ultra-violet gas laser at room temperature, Nature (London) **200**, 667 (1963).

[35] C. H. Li, A. J. Benedick, P. Fendel, A. G. Glenday, F. X. Kärtner, D. F. Phillips, D. Sasselov, A. Szentgyorgyi, and R. L. Walsworth, A laser frequency comb that enables radial velocity measurements with a precision of 1 $\mathrm{cm\,s^{-1}}$, Nature (London) **452**, 610 (2008).

[36] J. Hecht, Short history of laser development, Appl. Opt. **49**, F99 (2010).

[37] G. Makhov, C. Kikuchi, J. Lambe, and R. W. Terhune, Maser action in ruby, Phys. Rev. **109**, 1399 (1958).

[38] A. E. Siegman and H. J. Hagger, *Microwave Solid-State Masers* (McGraw-Hill, New York, 1964).

[39] K. Joshin, T. Mimura, M. Ninori, Y. Yamashita, K. Kosemura, and J. Saito, Noise performance of microwave HEMT, in *IEEE MTT-S International Microwave Symposium Digest* (IEEE, New York, 1983), pp. 563–565.

[40] M. Oxborrow, J. D. Breeze, and N. M. Alford, Room temperature solid-state maser, Nature (London) **488**, 353 (2012).

[41] J. D. Breeze, E. Salvadori, J. Sathian, N. M. Alford, and C. W. Kay, Continuous-wave room-temperature diamond maser, Nature (London) **555**, 493 (2018).

[42] T. Day, M. Isarov, W. J. Pappas, B. C. Johnson, H. Abe, T. Ohshima, D. R. McCamey, A. Laucht, and J. J. Pla, Room-temperature solid-state maser amplifier, Phys. Rev. X **14**, 041066 (2024).

[43] L. Jin, M. Pfender, N. Aslam, P. Neumann, S. Yang, J. Wrachtrup, and R. B. Liu, Proposal for a room-temperature diamond maser, Nat. Commun. **6**, 8251 (2015).

[44] See Supplemental Material at http://link.aps.org/supplemental/10.1103/6gn2-2v9b for S1: Dispersion relation for ring-shaped photonic time crystals. S2: Full-wave simulations of PTCs based on finite element methods. S3: Far-field calculations using angular spectrum theory. S4: Influence of ring-shaped PTC radius on the divergence angle of microwave lasing. S5: Comparative study between varactor diodes and multiplier-driven capacitors. S6: Detailed derivation of multiplier-driven time-varying capacitance. S7: Effective capacitances of the metamaterial structure. S8: Discrete space symmetry assisted far-field radiations of k-gap modes below the light line. S9: Modal coupling between CW and CCW k-gap modes in the discrete surface capacitance model. S10: Dependence on the number of discrete modulation units. S11: Sample fabrication and measurement methods. S12: Enhanced radiation intensity at ω due to the C6 symmetry breaking. S13: Phase noise and frequency stability of PTC-based lasing. S14: Comparison of the OAM beam purity of PTCs with other structures. S15: Quantitative breakdown of losses and energy efficiency. S16: Comparison with conventional masers and existing OAM emitters, which includes Refs. [45–55].

[45] Y. Y. Liu, T. R. Hartke, J. Stehlik, and J. R. Petta. Phase locking of a semiconductor double-quantum-dot single-atom maser, Phys. Rev. A **96**, 053816 (2017).

[46] E. N. Ivanov and M. E. Tobar, Low phase-noise sapphire crystal microwave oscillators: Current status, IEEE Trans. Ultrason. Ferroelectr. Freq. Control **56**, 263 (2009).

[47] Z. Zhang, S. Zheng, X. Jin, H. Chi, and X. Zhang, Generation of plane spiral OAM waves using traveling-wave circular slot antenna, IEEE Antennas Wireless Propag. Lett. **16**, 8 (2017).

[48] Z. Zhang, S. Xiao, Y. Li, and B. Z. Wang, A circularly polarized multimode patch antenna for the generation of multiple orbital angular momentum modes, IEEE Antennas Wireless Propag. Lett. **16**, 521 (2017).

[49] Y. Chen, S. Zheng, H. Chi, X. Jin, and X. Zhang, Half-mode substrate integrated waveguide antenna for generating multiple orbital angular momentum modes, Electron. Lett. **52**, 684 (2016).

[50] H. Li, L. Kang, F. Wei, Y. M. Cai, and Y. Z. Yin, A low-profile dual-polarized microstrip antenna array for dual-mode OAM applications, IEEE Antennas Wireless Propag. Lett. **16**, 3022 (2017).

[51] B. Liu, Y. Cui, and R. Li, A broadband dual-polarized dual-OAM-mode antenna array for OAM communication, IEEE Antennas Wireless Propag. Lett. **16**, 744 (2017).

[52] X. D. Bai, X.-L. Liang, Y.-T. Sun, P.-C. Hu, Y. Yao, K. Wang, J.-P. Geng, and R.-H. Jin, Experimental array for generating dual circularly-polarized dual-mode OAM radio beams, Sci. Rep. **7**, 40099 (2017).

[53] Q. Liu, Z. N. Chen, Y. Liu, F. Li, Y. Chen, and Z. Mo, Circular polarization and mode reconfigurable wideband orbital angular momentum patch array antenna, IEEE Trans. Antennas Propag. **66**, 1796 (2018).

[54] S. Long *et al.*, L-band milliwatt room-temperature solid-state maser, arXiv:2511.09056.

[55] H. Qin, R. Xiang, A. Jafargholi, Z. Zhang, and R. Fleury, Topological radiation from vortex masers, Nat. Commun. **16**, 10750 (2025).

[56] Forbes L. Mkhumbuza, and L. Feng, Orbital angular momentum lasers, Nat. Rev. Phys. **6**, 352 (2024).

[57] X. Cai, J. Wang, M. J. Strain, B. Johnson-Morris, J. Zhu, M. Sorel, J. L. O'Brien, M. G. Thompson, and S. Yu, Integrated compact optical vortex beam emitters, Science **338**, 363 (2012).

[58] Y. Lu, Y. Huang, J. Cheng, R. Ma *et al.*, Nonlinear optical physics at terahertz frequency, Nanophotonics **13**, 3279 (2024).